KURENAI 紅

Kyoto University Research Information Repository

KYOTO UNIVERSITY

Title	Polarization separated Zeeman spectra from magnetic dipole transitions in highly charged argon in the large helical device
Author(s)	Iwamae, A; Atake, M; Sakaue, A; Katai, R; Goto, M; Morita, S
Citation	Physics of Plasmas (2007), 14(4)
Issue Date	2007-04
URL	http://hdl.handle.net/2433/39796
Right	Copyright 2007 American Institute of Physics. This article may be downloaded for personal use only. Any other use requires prior permission of the author and the American Institute of Physics.
Type	Journal Article
Textversion	publisher

Kyoto University

Polarization separated Zeeman spectra from magnetic dipole transitions in highly charged argon in the large helical device

A. Iwamae,[a)] M. Atake, and A. Sakaue
Department of Mechanical Engineering and Science, Graduate School of Engineering, Kyoto University, Kyoto, 606-8501, Japan

R. Katai
Department of Fusion Science, Graduate University for Advanced Studies, Toki, 509-5292, Japan

M. Goto and S. Morita
National Institute for Fusion Science, Toki, 509-5292, Japan

Visible spectral emission lines from magnetic dipole transitions in Ar X, Ar XI, Ar XIV, and Ar XV are observed from plasmas heated with neutral-beam injection (NBI) in the Large Helical Device [O. Motojima *et al.*, Phys. Plasmas **6**, 1843 (1999)]. Orthogonal linearly polarized components of the emission line profiles are observed with a polarization separation optical system and high-resolution spectrometer. Zeeman split profiles reveal polarization characteristics of magnetic dipole transitions. Ion temperatures and emission locations are estimated from the profiles with the magnetic field information on the lines of sight (LOS). The spatially resolved emissions are observed by the array of absolutely calibrated views. The time histories of line profiles and emission intensities at the poloidal view are presented. The observed line profiles and the intensity distribution at the poloidal view indicate the localization of these charge states in the edge region just inside the last closed flux surface. The emission line of Ar X in the tangential observation indicates Doppler shifts of the Zeeman split profiles. The velocity components of Ar X ion flow along the LOS at the tangential view are 7.7 and 2.0 km/s at the outer and inner edge plasmas, respectively, in the opposite direction to the NBI. © *2007 American Institute of Physics*. [DOI: 10.1063/1.2714506]

I. INTRODUCTION

Since the first identification of electric-dipole-forbidden (magnetic-dipole and electric-quadrupole) transitions in the solar corona,[1] they have been observed in astrophysical and laboratory plasmas. Observations of electric-dipole-forbidden lines are summarized in Refs. 2 and 3. Recently, electron beam ion traps (EBITs) and heavy-ion storage rings have been used to investigate electric-dipole-forbidden transitions.[4–10] For magnetically confined plasmas, spectroscopic diagnostics by means of magnetic-dipole transitions have been pioneeringly performed on the Princeton Large Torus (PLT) tokamak with the emission lines in highly charged irons; Fe XX λ266.51 nm, Fe XVIII λ97.48 nm, and Fe XXII λ84.555 nm (Refs. 11 and 12). Such magnetic-dipole emission lines allow us to determine, e.g., the local ion temperature and density in high-temperature regions in the plasma.

The Large Helical Device (LHD) is a heliotron-type device. Long discharge duration of argon gas puffed plasmas is capable in the LHD. A vacuum ultraviolet emission line has been identified as a magnetic-dipole transition in Ar XII λ64.903 nm ($2s^2 2p^3\ ^4S_{3/2} \leftarrow\ ^2P_{3/2}$) and emission lines in the visible region observed with low-resolution spectrometers have been verified as magnetic-dipole transitions: Ar X

λ553.3 nm ($2s^2 2p^5\ ^2P^o_{3/2} \leftarrow\ ^2P^o_{1/2}$:M1), Ar XI λ691.7 nm ($2s^2 2p^4\ ^3P_2 \leftarrow\ ^3P_1$) with a weak electric quadrupole admixture, Ar XIV λ441.3 nm ($2s^2 2p\ ^2P^o_{1/2} \leftarrow\ ^2P^o_{3/2}$) and Ar XV λ594.4 nm ($2s2p\ ^3P^o_1 \leftarrow\ ^3P^o_2$) (Ref. 13). Wavelengths of these visible magnetic-dipole transitions are determined with high precision by means of the EBIT (Ref. 8). Spectroscopy on argon ion in x-ray, extreme ultraviolet (EUV), and visible spectral ranges are reviewed in Ref. 8. The measured transition rates of Ar X ($2s^2 2p^5\ ^2P^o_{3/2} \leftarrow\ ^2P^o_{1/2}$), Ar XI ($2s^2 2p^4\ ^3P_2 \leftarrow\ ^3P_1$), Ar XIV ($2s^2 2p\ ^2P^o_{1/2} \leftarrow\ ^2P^o_{3/2}$), and Ar XV ($2s2p\ ^3P^o_1 \leftarrow\ ^3P^o_2$) are reported to be (107.3 ± 1.4) s^{-1} (Refs. 6 and 7), (67.6 ± 2.2) s^{-1} (Refs. 4 and 5), (104.46 ± 0.04) s^{-1} (Ref. 10), and (65.9 ± 3) s^{-1} (Refs. 6 and 7), respectively. The theoretical lifetime 14.99 ms of the transition Ar XI ($2s^2 2p^4\ ^3P_2 \leftarrow\ ^3P_1$) cited in Ref. 14 is in good agreement with the experiment (14.8 ± 0.48) ms (Refs. 4 and 5). For the Ar XV $2s2p\ ^3P^o_2$ level, the 1.2% magnetic quadrupole decay to the singlet ground state $2s^2\ ^1S_0$ is taken into account.[6]

Doppler shifts of emission lines are measured with high-resolution spectroscopy in the divertor and the peripheral regions of tokamaks and helical devices. In the Axially Symmetric Divertor Experiment (ASDEX) upgrade plasma, the C^{2+} ions (C III λ229.7 nm) are found to flow at a speed of 10 km/s in the *L* mode and 10–20 km/s in the edge localized mode (ELM) *H*-mode phases.[15] On the Doublet III-D normal flows towards the target plate $(2-14$ km/s) and reverse flows away from the target plate $(5-30$ km/s) are de-

tected from C II (λ658.0 nm) and C III (λ464.9 nm) spectral lines.[16] Neutral deuterium flow of 5 km/s has been measured in the Alcator C-mod plasma.[17] The Dα (λ656.1 nm) line spectral profiles emitted from the divertor region of the Japan Atomic Energy Research Institute Tokamak-60 Upgrade (JT-60U) plasma are observed with high-resolution spectrometer and examined by means of a neutral particle transport code.[18,19] Selective polarized σ components of the Zeeman profiles in O V (in second order of λ278.7 nm), Hα (λ656.3 nm), and He I (λ587.6 nm) are used to measure ion and neutral temperatures and neutral flow velocities in the Torus of Research Institute for Applied Mechanics (TRIAM-1M) plasma.[20,21]

The simultaneous observation on the orthogonal polarized components has been found useful to determine the emission location, temperature, and inward velocities (1–7 km/s) of neutral hydrogen in peripheral plasmas confined in the LHD.[22] In a high ion temperature plasma with negative-ion-based neutral-beam injection (NBI) heating with Ar gas fueling, toroidal flow velocities close to 50 km/s in the core plasma have been evaluated from the resonance line in helium-like argon Ar XVII with a high-resolution x-ray crystal spectrometer.[23,24] In this paper we combine a high-resolution spectrometer with a polarization separation technique in order to obtain information on the plasma by measuring spectral line profiles of the magnetic-dipole transitions in fluorine-like Ar X, oxygen-like Ar XI, boron-like Ar XIV, and beryllium-like Ar XV.

II. EXPERIMENTAL SETUP

Figure 1 shows a schematic view of the LHD from the top. The major and minor radii are 3.9 and 0.6 m, respectively. A pair of superconducting helical coils and three pairs
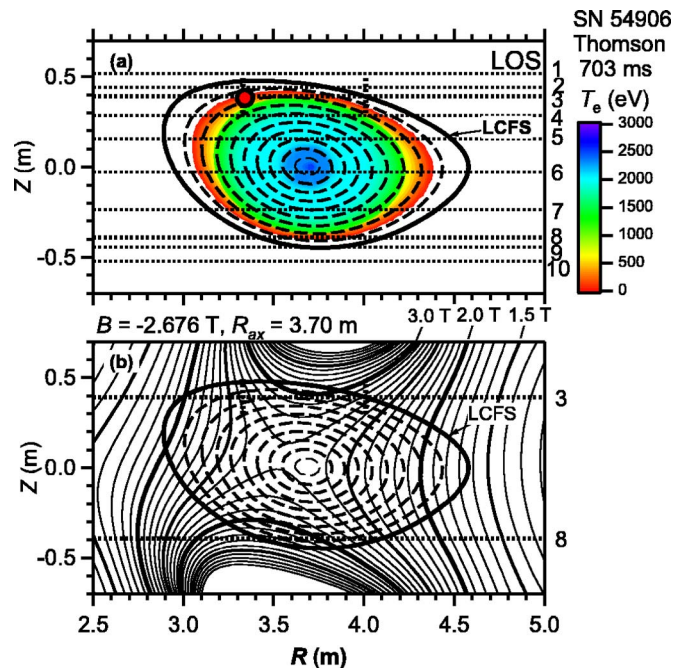
FIG. 2. (Color online) (a) A map of the flux surfaces for the configuration of magnetic axis position R_{ax}=3.70 m. The contour plot of the electron temperatures measured by means of Thomson scattering for the shot number 54 906 at 703 ms with an assumption of the symmetry on the normalized minor radius ρ. The ordinate R and the abscissa Z indicate the major radial direction and the direction perpendicular to the equatorial plane, respectively. The ten lines of sight (LOS) are shown with horizontal dotted lines of the present polarization separation observation. (The plotted LOS positions are for the 62 409). The circle on LOS 3 indicates the location of the Ar XIV emission in exposure from 0.612 s with the duration of 0.231 s. (b) A map of the magnetic field strength of B_{ax}=−2.676 T. LOS 3 (Z=+0.391 m) and LOS 8 (Z=−0.391 m) are indicated with thick dotted ,lines where intensities of the emission lines of the magnetic dipole transitions are relatively high.

of superconducting vertical field coils produce a helical field of poloidal winding number l=2 and toroidal field period m=10 (Ref. 25).

For the argon discharge experiment, the direction of the magnetic field was counterclockwise, which was represented by the negative sign of B. The argon-puffed plasma for high ion temperature experiments were carried out mainly at a magnetic field strength B_{ax}=−2.676 T at the axis radius R_{ax}=3.70 m. Argon glow discharge cleaning and titanium gettering were performed before the argon-puffed shots to suppress dilution of the highly ionized plasma with wall-absorbed hydrogen. The plasma was produced with NBI. The NBI system in the LHD consisted of three tangential injectors, each of which had two beams from negative-ion sources.[26] The beam species was hydrogen. The nominal injection energy was 180 keV. The emission radiation from the plasma was collected from the poloidal direction at the 1-O port tilted at 6° with respect to the poloidal cross section as shown in Fig. 1. At the 1-O port cross section, as depicted in Fig. 2(a), ten lines of sight (LOS) were aligned in the vertical plane. The cross section of the plasma was elongated in the major radius direction.

Since the plasma current is virtually absent, the coil currents determine the magnetic field distribution in the plasma. In the confinement region the field lines form closed mag-
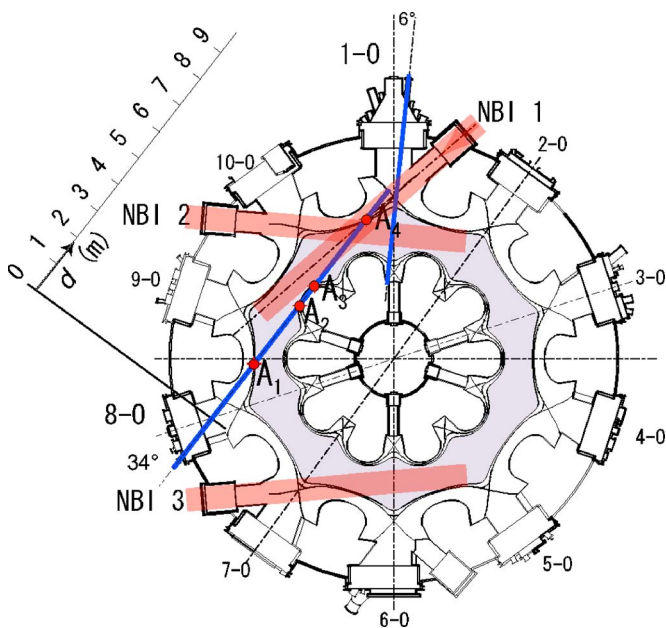

FIG. 1. (Color online) Top view of the Large Helical Device. The lines of sight (LOS) through the 1-O and 8-O ports are shown in solid lines. The NBI 1 and 3 are the counterclockwise injection. The NBI 2 is the clockwise injection. The emission locations on the tangential view from the 8-O port are referred to as A_1, A_2, A_3, and A_4.

netic surfaces and the outermost surface is called the last closed-flux surface (LCFS), where the normalized minor radius $\rho = r/a_{LCFS} = 1$. Vacuum magnetic flux surfaces are obtained based on the Biot-Savart law with a highly accurate numerical procedure.[27,28] The magnetic field structure and confinement of energetic particles are investigated with a suite computing code.[29] Figure 2(b) shows a map of the magnetic field strength at the cross section. The magnetic field structure is saddle shaped and the field strength near the helical coils is high.

Beam-splitting Glan-Thompson polarization separators were used to observe the emission except at the LOS 6 ($Z = -0.026$ m). In a Glan-Thompson prism, optical cement used to make the two calcite prisms contact absorbs UV light; the Glan-Thompson polarization separator transmits light above the wavelength of 300 nm as an extraordinary-ray component. An ordinary-ray component is reflected at 45° on the contact surface with respect to the incident light axis. The polarization direction of the reflected light is parallel in the plane including the incident and reflected directions. The extraordinary-ray component or the light polarized perpendicular to the plane is transmitted undeviated. At the center LOS 6 ($Z = -0.026$ m), we used a Glan-Taylor-type polarization separation optical system.[22] An air spaced Glan-Taylor polarizer transmits the light in the UV light from the wavelength of 220 nm. Both polarization separators are designed and aligned so that each of the orthogonally polarized components comes from the same LOS. The field of view of the LOS had a diameter of 55, 68, and 84 mm at the outer, central, and inner observation regions, respectively. Figures 3(a)–3(c) show the variation of the magnetic field vectors $\boldsymbol{B}$ along LOS 3 ($Z = +0.391$ m) and LOS 8 ($Z = -0.391$ m): (a) the magnetic field strength B and (b) the pitch angle θ of the magnetic field from the horizontal plane, and (c) the yaw angle ϕ between the projection of the magnetic field vector on the horizontal plane and the perpendicular direction to the LOS. On LOS 3 and 8, emission intensities of the magnetic-dipole transitions are relatively high, as can be seen later.

Another LOS was oriented approximately along the tangential direction through the 8-O port tilted at 34° with respect to the radial direction at the center of the 8-O port as shown in Fig. 1. The tangential LOS was in the horizontal plane at a height of $Z = 0.020$ m, slightly above the equatorial plane. A lens coupler was used. The polarization was unresolved at the tangential viewing chord. Figures 3(d)–3(f) show the variation of the magnetic field vector $\boldsymbol{B}$ along the tangential LOS. The abscissa is the distance d from the origin along the LOS where the radial line crosses the LOS as shown in Fig. 1. The plasma emission was transmitted by means of a bundle of 24 quartz optical fibers with 400 μm core. One of the optical fibers was used to record emission lines from a Th-Ar hollow cathode lamp as the wavelength reference.[30]

The light transmitted through the optical fibers was led to a Czerny-Turner-type spectrometer ($f = 1.33$ m, 1800 grooves/mm holographic grating). The entrance slit width was 20 μm. The light dispersed by the grating was recorded with a charge-coupled device (CCD) camera: 1024×1024, 13 μm square pixels). The linear dispersion
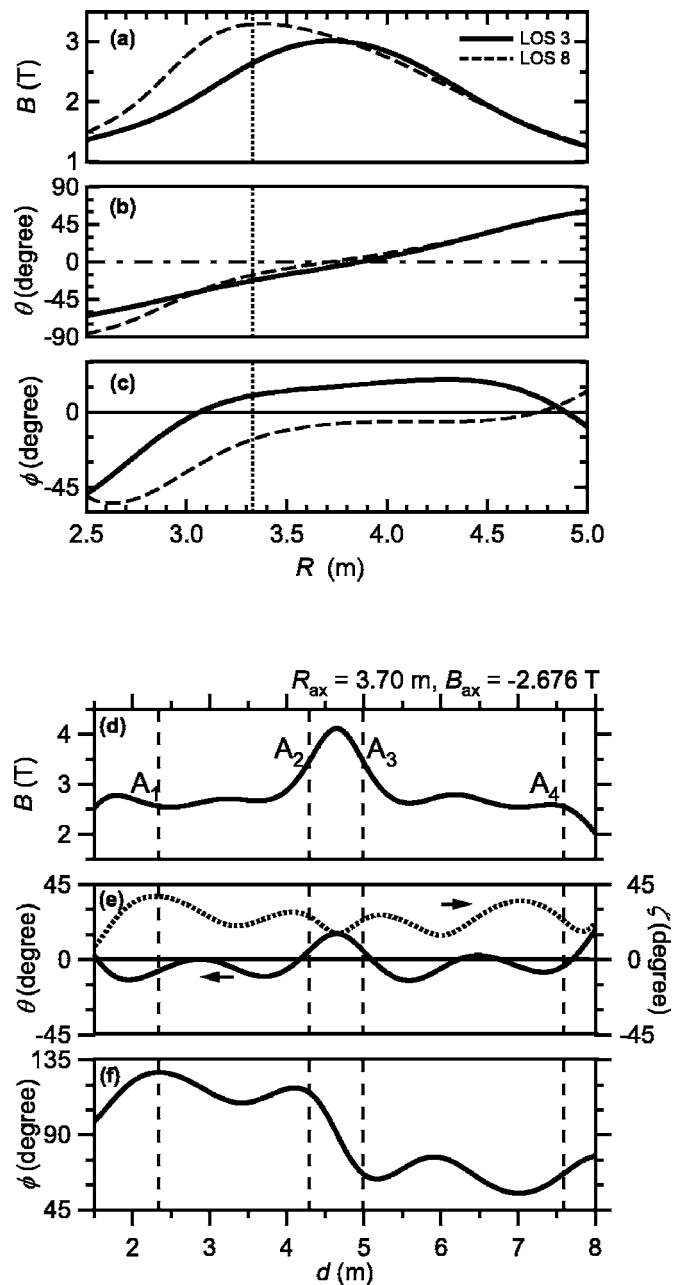

FIG. 3. Magnetic field information on the (a)–(c) poloidal and (d)–(f) tangential views. (a) Variation of the magnetic field strength on LOS 3 (solid curves) and LOS 8 (dashed curves). (b) Pitch angles θ of the magnetic field with respect to the horizontal plane. (c) Yaw angles ϕ between the projection of the magnetic field vector on the horizontal plane and the plane perpendicular to the line of sight. (d) Variation of the magnetic field strength on tangential line of sight from the 8-O port. (e) Pitch angle θ. (f) Yaw angle ϕ. The emission locations on the tangential view are referred to as A_1, A_2, A_3, and A_4.

was 0.366 nm/mm at $\lambda 441.3$ nm in the first order. The instrument function was well represented with a Gaussian profile. The full width at half maximum was 0.011 nm or 2.33 pixels. The CCD detector was electrically cooled down to $-20\,°$C with Peltier device for the purpose of reducing thermal noise. The typical exposure time was 231 ms with the repetition frequency of 4 Hz. The observed intensity was absolutely calibrated with a tungsten-halogen spectral irradiance lamp (USHIO JPD100V-500WCS) and a white reflec-

tance diffuse plate (Labsphere Spectralon: SRS-99-020). The spectral irradiance of the lamp in the units of (W/m² nm) at the distance 500 mm was given by the manufacturer. The white plate diffusely reflected the incident light into a hemisphere (2π sr). The wavelength dependence of the reflectance was also provided.

III. RESULTS AND DISCUSSION

Figures 4(a) and 4(b) show time evolutions of the typical discharge parameters in argon-puffed plasma for high ion temperature of the shot number 54 902 and 62 409, respectively. Peak values of the line-averaged electron density for the argon discharges on which we observed the magnetic-dipole emission lines ranged from 1 to 1.5×10^{19} m^{-3}. Electron temperatures at the center of the plasma were 3–5 keV. The ion temperature, which was derived from the Doppler broadening of a He-like resonance line of Ar XVII, reached 10 keV (Refs. 23 and 24). For the shot number 62 409 shown in Fig. 4(b), the clockwise direction neutral beam, NBI 2, at the 10-T (tangential) port, starts a plasma discharge at 0.3 s, which is a counterinjection beam relative to the helical coil current. Argon gas is puffed from the 3.5-L, 0.5 s with a valve opening time of 7.4 ms, which is plotted at the bottom of Fig. 4. The plasma is additionally heated with the counterclockwise direction beams, NBI 1 and NBI 3. The duration of the NBI heating is 2 s. The diamagnetic stored energy W_p gradually increases as a function of time at the initial phase of the NBI heating. After reaching a maximum of 470 kJ, W_p slightly decreases and remains constant around 320 kJ. The electron density distribution is measured at the 8.5 port with ten channels of 118.8 μm CH$_3$OH laser inter-
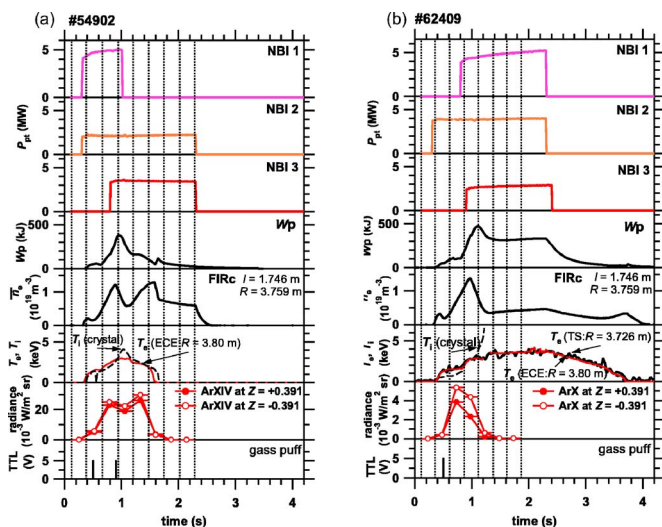

FIG. 4. (Color online) Time evolutions of the injection power P_{pt} of the NBI 1, 2, and 3; the plasma stored energy W_p; the line-averaged electron density $\overline{n}_e$; the ion and electron temperatures T_i and T_e from the top for a high ion temperature plasma with argon gas puffing for the shot numbers (a) 54 902 and (b) 62 409: The radiances of the Ar X emission observed on LOS (Z = +0.391 m) and (Z = −0.391 m) are plotted. (a) Argon gas was puffed at 0.5 and 0.9 s with valve opening times of 6.8 and 6.0 ms, respectively. The emission in Ar XIV is obtained on a successive five frames. (b) Argon gas was puffed at 0.5 s with a valve opening time of 7.4 ms. The radiance is high enough to analyze the line profiles in two frames for the exposures from 0.612 and 0.863 s. The ion temperatures after 1.22 s are unavailable.

ferometer. The line-averaged electron density $\overline{n}_e$ at the near central chord of the channels is plotted. After an increase in the electron density due to Ar gas puffing, the central ion temperature, measured with Doppler broadening of the resonance line of helium-like Ar XVII, rapidly increases as the density decreases. The electron temperature, estimated from electron cyclotron emission (ECE) measurements, gradually increases up to 3.9 keV. It is much lower than the ion temperature. The electron temperature provided by means of yttrium aluminum garnet (YAG) Thomson scattering agrees well with the ECE measurements. The intensities of Ar X emission lines observed at LOS 3 (Z = +0.391 m) and LOS 8 (Z = −0.391 m) reach a maximum at the frame from 0.612 s with 0.231 s exposure time with the repetition rate of 4 Hz.

The electron and ion temperatures showed extremely slow decay after the NBIs turnoff as shown in Fig. 4(b). The beam slowing-down time was long. Although the NBI heating sustained the plasma of 2 s, the magnetic-dipole emissions were observed at the limited time regions like those shown in Fig. 4(b). The main species of the plasma were argon and hydrogen. From the measurement of recombination Hα intensity at the plasma termination,[31] the hydrogen ion density was estimated to be 25–40% of the electron density.

For shot number 54 902 shown in Fig. 4(a), argon gas puffs at 0.5 and 0.9 s with valve opening times of 6.8 and 6.0 ms, respectively, prevent an increase in the ion temperature. It peaked around 4 keV. While the electron density is kept relatively high compared to that of shot number 62 409, the emission in Ar XIV is observed on a successive five frames with an exposure time of 250 ms at the repetition rate of 3.7 Hz, and the intensities of Ar XIV reach their maximum at the frame from 0.612 s.

Figure 5 shows an example of the polarization separated spectra from an argon plasma observed at LOS 3 (Z = +0.391 m). The emission from the plasma through the polarization separator was resolved into two orthogonal polarized beams: ordinary ray (o ray) and extraordinary ray (e ray). The orthogonal linearly polarized components were chosen at 76° (ordinary ray) and 166° (extraordinary ray) directions with respect to the horizontal plane. Each of the directions is indicated with a line in a circle in Fig. 5. For electric-dipole transitions in Ar II, line profiles show a characteristic anomalous Zeeman splitting pattern. For example, the Zeeman split line, Ar II λ442.6 nm ($4s\ ^4P_{3/2} - 4p\ ^4D_{5/2}$) shows the two split peaks in the 76° component and single peak in the 166° component. The two split peaks dominantly consist of magnetic sublevel to magnetic sublevel transitions of $\Delta M = M' - M = \pm 1$, where M and M' are the magnetic quantum numbers of the lower and upper levels. The ΔM = ±1 transitions are the σ light, the oscillating electric field vector of which is perpendicular to the magnetic field direction or the quantization axis when the observation direction is normal to the quantization axis. The peak of the 166° component is located at the center wavelength between the two peaks of the σ-light component. This peak dominantly consists of $\Delta M = 0$ transitions or the π light, the oscillating electric field vector of which is parallel to the quantization axis.
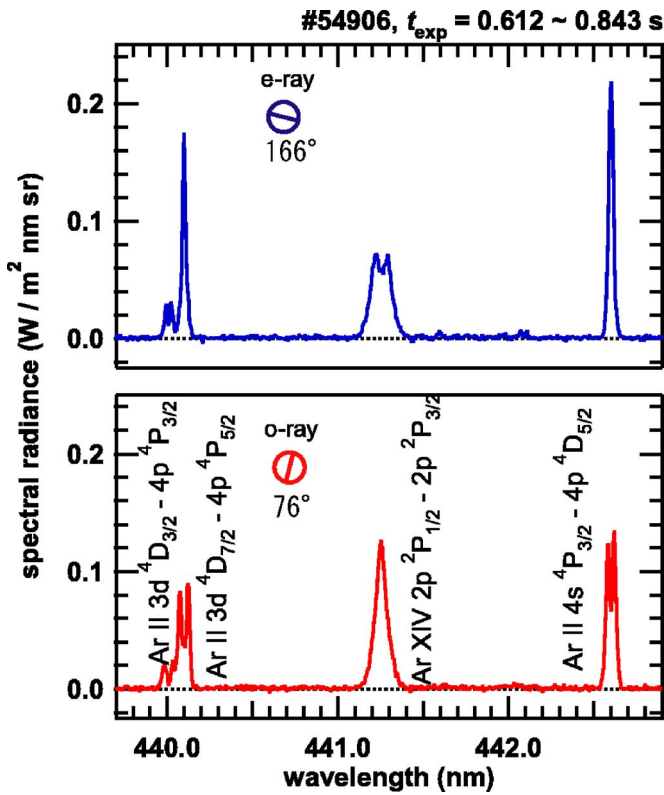
FIG. 5. (Color online) Line profiles of electric-dipole transitions Ar II and a magnetic-dipole transition Ar XIV spectra. Emissions are separated into orthogonal linearly polarized light, i.e., the 166° (e-ray) component and the 76° (o-ray) component. The angle of the linear polarization components is measured with respect to the horizontal plane. The polarized light in the 166° and 76° directions are approximately parallel and perpendicular to the magnetic field direction, respectively.

FIG. 6. (Color online) Polarization separated Zeeman profiles of the magnetic-dipole emission lines observed on LOS 3: (a) Ar X λ553.3 nm $(2s^2 2p^5 \ ^2P^o_{3/2} \leftarrow {}^2AP^o_{1/2})$; (b) Ar XI λ691.7 nm $(2s^2 2p^4 \ ^3P_2 \leftarrow {}^3P_1)$; (c) Ar XIV λ441.3 nm $(2s^2 2p \ ^2P^o_{1/2} \leftarrow {}^2P^o_{3/2})$; and (d) Ar XV λ594.4 nm $(2s2p \ ^3P^o_1 \leftarrow {}^3P^o_2)$. Observed line profiles are fitted with an assumption of a single ion temperature at an emission location on the line of sight. Kastler diagram of the transitions between Zeeman split magnetic sublevels to magnetic sublevels are shown under the corresponding spectra.

A broad line is seen at λ441.3 nm, which shows two split peaks in the 166° polarized component and a central peak at the 76° polarized component. This splitting feature is in contrast to the line profile of the electric-dipole transitions. This line is assigned as a magnetic-dipole transition between levels in the ground-state configuration of boron-like argon Ar XIV $(2s^2 2p \ ^2P^o_{1/2} \leftarrow {}^2P^o_{3/2})$. From a classical point of view, the oscillating magnetic dipole along the quantization axis emits light; this corresponds to the $\Delta M=0$ transitions. The oscillating magnetic field vector of the light from the $\Delta M =0$ transitions is parallel to the quantization axis and its polarization direction is *perpendicular* to the quantization axis, since polarization is defined by the direction of the electric field vector. The $\Delta M=\pm 1$ transitions in the magnetic-dipole transition are also classically illustrated as a circular motion either clockwise or counterclockwise in the plane perpendicular to the quantization axis. Looking from the positive direction, $\Delta M=+1$ and -1 transitions are the clockwise and counterclockwise circularly polarized light in the plane. More generally, the radiation is elliptically polarized. When viewed from a point in the plane perpendicular to the quantization axis, the magnetic dipole oscillates perpendicularly to the quantization axis and its radiation is linearly polarized *parallel* to the quantization axis. As shown in Figs. 3(a)–3(c), the magnetic field direction is almost horizontal and perpendicular to the LOS 3 around $R=3.3$–4.0 m. We
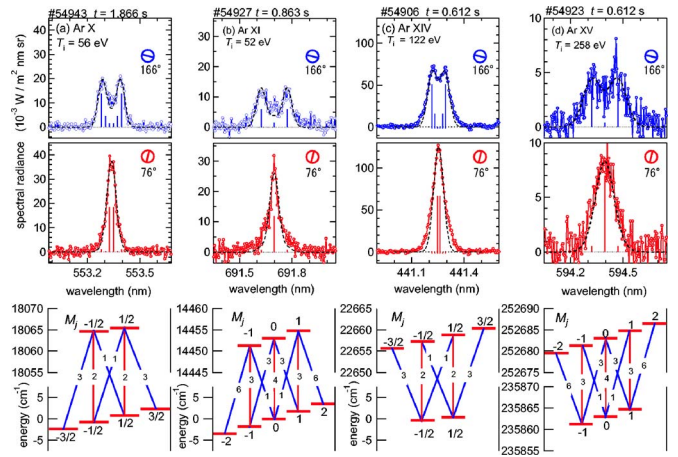
observe similar contrast of the polarization characteristics of the magnetic-dipole transitions. Figure 6 shows the polarization-resolved line profiles for the Zeeman splitting of magnetic-dipole transitions: Ar X λ553.3 nm $(2s^2 2p^5 \ ^2P^o_{3/2} \leftarrow {}^2P^o_{1/2})$, Ar XI λ691.7 nm $(2s^2 2p^4 \ ^3P_2 \leftarrow {}^3P_1)$, Ar XIV λ441.3 nm $(2s^2 2p \ ^2P^o_{1/2} \leftarrow {}^2P^o_{3/2})$ and Ar XV λ594.4 nm $(2s2p \ ^3P^o_1 \leftarrow {}^3P^o_2)$.

Since the Zeeman splitting of a level for observed magnetic-dipole transitions is much smaller than the fine-structure splitting, the energy shift W of a magnetic sublevel in a magnetic field B is well described by the anomalous Zeeman effect,

$$W = g\mu_B M B, \tag{1}$$

where μ_B and g are the Bohr magneton and the Landé g factor, respectively. A formula for the Landé g factor is given by

$$g = 1 + (1+2a)\frac{J(J+1)+S(S+1)-L(L+1)}{2J(J+1)}. \tag{2}$$

We assume $a=0$ in the following.

The transition probability from an upper state $\gamma'J'M'_J$ to a lower state $\gamma J M$ is expressed as

$$
\begin{aligned}
a_{M1} &= \frac{16\pi^3 e^2 a_0^2 (\alpha/2)^2 \sigma^3}{3\varepsilon_0 h(2J'+1)} \sum_q |\langle \gamma J M \| \mathbf{J}^{(1)}_q + \mathbf{S}^{(1)}_q \| \gamma' J' M' \rangle|^2 \\
&= \frac{16\pi^3 e^2 a_0^2 (\alpha/2)^2 \sigma^3}{3\varepsilon_0 h(2J'+1)} \sum_q \begin{pmatrix} J & 1 & J' \\ -M & q & M' \end{pmatrix}^2 |\langle \gamma J \| \mathbf{J}^{(1)} \\
&\quad + \mathbf{S}^{(1)} \| \gamma' J' \rangle|^2,
\end{aligned} \tag{3}
$$

where a_0 is the first Bohr radius, α the fine-structure constant, σ the wave number of the line, and ε_0 the vacuum permittivity.[32] Selection rules for J and M, and the relative strengths of the line components for a magnetic-dipole tran-
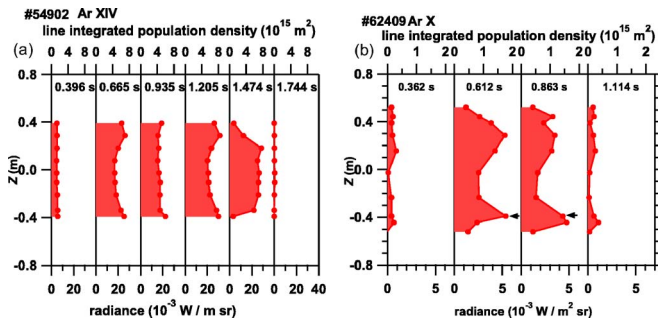
FIG. 7. (Color online) Time histories of emission intensities of the (a) Ar XIV λ441.3 nm and (b) Ar X λ553.3 nm at the poloidal view obtained in shot numbers 54 902 and 62 409, respectively.

TABLE I. The parameters obtained from fitting: ion temperature T_i, magnetic field strength $B(R)$, and emission location R at the line of sight (Z = +0.391 m). * The variation range of the electron temperature T_e at the equivalent normalized radius during the exposure time obtained by means of the Thomson scattering measurement.

	Ar X	Ar XI	Ar XIV	Ar XV
T_i (eV)	56±6	52±6	122±9	258±45
B (T)	2.36±0.04	2.20±0.04	2.64±0.04	2.90±0.10
R (m)	3.18±0.02	3.10±0.02	3.33±0.03	3.52±0.12
T_e(eV)*	120–540	240–620	260–650	150–650

sition are exactly the same as for an electric-dipole transition, because the 3-*j* symbol in Eq. (3) is common for magnetic-dipole and electric-dipole transitions. Kastler diagrams from the magnetic sublevels to the magnetic sublevels[32,33] are illustrated at the lower part of Fig. 6. The intensity distributions of the emission radiation for $\Delta M = -1, 0$ and +1 are proportional to $1/2(1+\cos^2 \zeta)$, $\sin^2 \zeta$, and $1/2(1+\cos^2 \zeta)$, respectively, where ζ is the polar angle with respect to the magnetic field direction. The angle ζ is related to the pitch and yaw angles, θ and ϕ, of the magnetic field vectors **B** plotted in Figs. 3(b) and 3(c) or Figs. 3(e) and 3(f) as

$$\cos \zeta = \cos \theta \sin \phi. \qquad (4)$$

Now the X axis is defined in the horizontal directions so that the X-Z plane is normal to the LOS (see Fig. 7 in Ref. 21). The projection of the **B** vector onto this plane makes an angle η with respect to the vertical Z axis, which is given by

$$\tan \eta = \cot \theta \cos \phi. \qquad (5)$$

In order to fit the observed Zeeman profile we assume that the emission locations of argon ions are localized at a single point on the LOS and that the profile is given by a single ion temperature T_i. The major radius R of the emission location is the parameter of the line profiles via the magnetic field vector, B, θ, and ϕ, whose dependences on R are well described with polynomial functions of sixth order (seven parameters for each of B, θ, and ϕ). The Zeeman split line profiles for the orthogonal polarization directions are fitted with parameters of line intensity I_0, line center wavelength λ_0, Doppler width T_i, and $B(R)$. The results of the fitted profiles are plotted with the dashed curves in Fig. 6. In reproducing the split peaks we exclude the broad wing part of the spectral profiles, so that there remains a discrepancy in the wings [see Fig. 6(c), for instance].

There are two candidates for the emission location R on the line of sight from the fitted line profile since the magnet field strength curve has the same B value at two locations as shown in Fig. 3(c). For example, $B = 2.64 \pm 0.04$ T gives good convergence of fitting for the Ar XIV λ441.3 nm line profile shown in Fig. 6(c). As shown in Fig. 3(a) the B value leads to $R_{in} = 3.33 \pm 0.03$ m and $R_{out} = 4.01 \pm 0.02$ m. At the inner location R_{in}, the LOS crosses the surface of normalized minor radius $\rho = 0.85$, and R_{out} the surface of $\rho = 1.0$. Figure 2(a) shows the electron temperature distribution at $t = 703$ ms ob-

tained by means of the Thomson scattering measurements.[34] It is seen that, at $\rho = 1.0$, the temperature is too low to ionize the ions to this ionization stage. Thus we conclude that the inner point $R_{in} = 3.33 \pm 0.03$ m is the valid candidate of the emission location, which is marked with a circle on LOS 3 in Fig. 2(a). An ion temperature of 122 eV with 8% uncertainty of the fitting reproduces the Zeeman split peaks. The discrepancy between the fitted and observed profiles may be ascribed to two origins. Firstly, the actual emission location may be distributed around the surface of $\rho = 0.85$, and the higher magnetic field components along the surface near $R = 3.8$ m may contribute to the profile. Secondly, we accumulate the spectral intensity with a relatively long exposure time of 231 ms during increasing T_i in the observed region. The ion temperature also increases during this time duration. The spectra shown in Fig. 6(c) suggest that the latter explanation is more plausible.

The emission locations and ion temperatures are determined also for the Ar X λ553.3 nm, Ar XI λ691.7 nm, and Ar XV λ594.4 nm lines, whose profiles are shown in Figs. 6(a), 6(b), and 6(d), respectively. The results of the fit are tabulated in Table I. Similar ion temperatures of 56 and 52 eV are obtained for Ar X and Ar XI, respectively. The ion temperatures for Ar XIV and Ar XV are 122 and 258 eV, respectively.

The time histories of the intensity distribution at the poloidal view for Ar XIV λ441.3 nm and Ar X λ553.3 nm are plotted in Figs. 7(a) and 7(b). The LOS positions for shot number 54 902 are slightly different from that for 62 409. Although the observed emission region in the poloidal view is limited from $Z = +0.391$ to -0.391 m in shot number 54 902, the emission distributions profile of Ar XIV at the second frame exposed from 0.665 s is similar to that for the Ar X obtained in shot number 62 409. At the third frame (0.935 s) the center ion temperature reaches the peak temperature as presented in Fig. 7(a). It can be seen from the intensity distribution that the emission distribution of Ar X is localized in the more outer region compared to the second (0.665 s) and fourth (1.205 s) frames. Then emission region is considered to shrink toward the axis at the fifth frame (1.474 s) with a decrease in the ion and electron temperatures. The emission intensities of Ar X λ553.3 nm observed in shot number 62 409 are high enough to analyze the line profiles in two frames for the exposures from 0.612 and 0.863 s as shown in Fig. 7(b). The observed intensity distributions are peaked at LOS 4 ($Z = +0.286$ m) and LOS 8
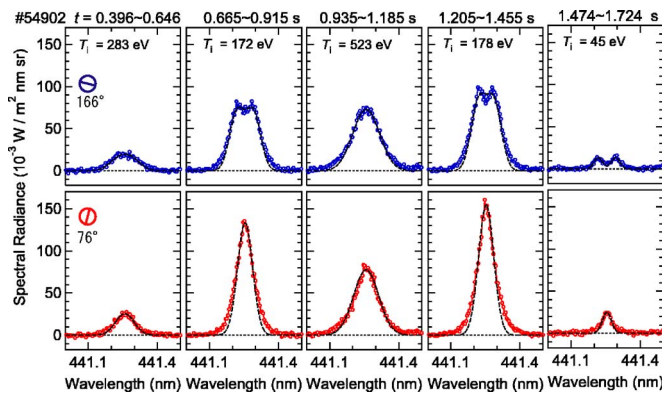
FIG. 8. (Color online) The results of fitting over time alongside time histories of the emission Ar XIV λ441.3 nm lines at $Z=-0.391$ m from the poloidal view for shot number 54 902. Relevant discharge parameters are shown in Fig. 4(a).

FIG. 9. (Color online) Ar X λ553.3 nm profiles exposed from 0.612 s with 231 ms exposure time observed (a) on LOS 8 ($Z=-0.391$ m) at the 1-O port. Polarized components of 0° and 90° directions are plotted in the upper and lower panels, respectively; (b) from tangential line of sight at the 8-O port. The fitted curves are plotted with the solid curves; (c) and (d) at the successive exposure time from 0.863 s. Relevant discharge parameters are shown in Fig. 4(b).

($Z=-0.391$ m) at the exposure from 0.612 s. The intensity distribution of the upper half is broader in the vertical direction than that of the lower half. The emission distribution suggests that Ar X and XIV ions are localized in the outer region just inside the LCFS. These time histories of the intensity distribution will be a subject for future investigations.

The time histories of the line profiles of Ar XIV λ441.3 nm on the LOS at $Z=+0.391$ are shown in Fig. 8. No tangential LOS was available in this shot. At the first frame (0.396 s) the density is low and the ion temperature derived from Ar XIV spectra is 283 eV. With an increase in the electron density, it decreases to 172 eV at the second frame (0.665 s); then, it increases to 523 eV at the third frame (0.935 s), where the central ion temperature peaks and the electron density sags. At the fourth frame (1.205 s) it decreases to 178 eV and at the fifth frame (1.474 s), relatively low temperature 45 eV is observed.

The time histories of the line profiles of Ar X λ553.3 nm on LOS 8 ($Z=-0.391$ m) at the 1-O port are shown in Figs. 9(a) and 9(c), and on the tangential line of sight at the 8-O port in Figs. 9(b) and 9(d). At LOS 8 in Figs. 9(a) and 9(c), the emission is separated into two linearly polarized components at 0° horizontal and 90° vertical directions. The estimated emission locations are either $R=3.47\pm0.03$ or 3.99 ± 0.04 m for Fig. 9(a) from the fitting with the magnetic field vector **B** on LOS 8 shown in Figs. 3(a)–3(c). Actually, both emission locations may contribute to the line profiles. The peak profiles are narrow and the estimated ion temperature is 8 eV. For Fig. 9(c) the location $R=3.86\pm0.22$ m converged with ion temperature of 70 eV. The line profiles observed from the tangential view shown in Figs. 9(b) and 9(d) represent the dominant $\Delta M=\pm1$ components. The vertical dash-dot lines indicate the center wavelength determined from the emission peaks in the 90° polarized component, $\lambda_0=553.327$ nm. This center wavelength is consistent with the reported value of $\lambda_0=553.3265$ nm, which is determined by the in the EBIT experiment.[8] Little Doppler shift is present on LOS 8 in Figs. 9(a) and 9(c). This absence of the Doppler shift is common to all the poloidal view at the observed exposures. The parameters of the magnetic field vector **B** on the tangential view as shown in Figs. 3(d)–3(f)
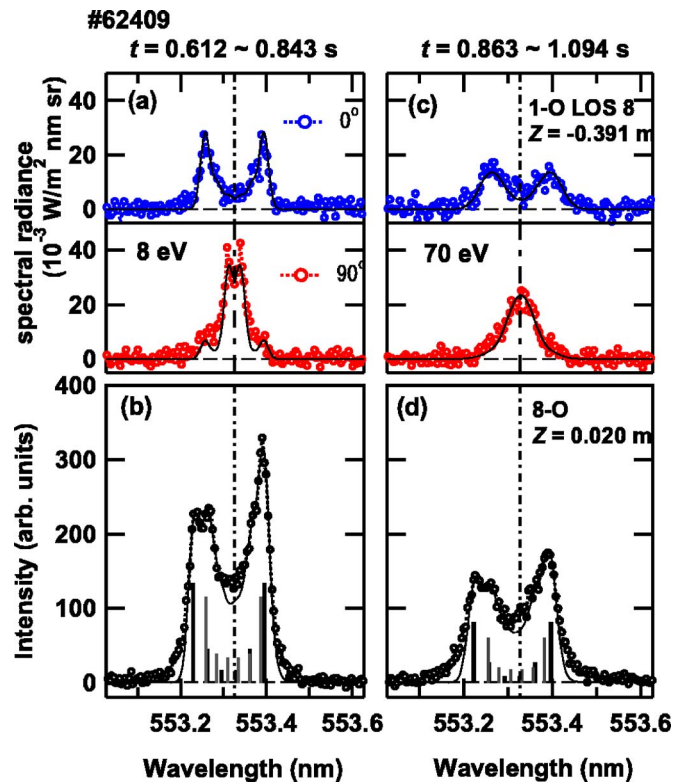
indicate that we observe the emission close to the parallel direction with respect to the magnetic field, $\phi\sim0°$. The line profiles in Figs. 9(b) and 9(d) are asymmetric: the peak on the shorter wavelength side shows a doublet structure and the height of the peak on the longer wavelength side is higher than that of the shorter one. This suggests that the longer-wavelength peak is a superposition of two peaks. Further, the center wavelengths of both pairs of the peaks are shifted to the shorter wavelengths. We interpret these features as due to the different Doppler shifts from the ions radiating at different magnetic field strengths. From the observation at the 1-O port, the Ar X emission is found to be localized at the edge region around $\rho=0.8\sim0.9$. We assume toroidal symmetry on the ion density distribution. Four points A_1, A_2, A_3, and A_4 plotted on the tangential line of sight in Figs. 1 and 3(d)–3(f), where the tangential LOS crosses the edge region, are considered to be the emission locations. The points A_2 and A_3 are at the higher magnetic fields and A_1 and A_4 are at the lower magnetic fields. The fitting does not converge with the four emission locations parametrized simultaneously. Then, we choose a pair of higher and lower magnetic fields (A_1, A_2) or (A_3, A_4)) as the locations to perform least-squares fitting with a set of parameters of distances d_H and d_L from the origin to the emission locations, ion temperatures T_{iL} and T_{iH}, and Doppler shifts velocity v_{DL} and v_{DH}. An example of the fitting results is shown with the solid curves

in Figs. 9(b) and 9(d). The profile in Fig. 9(b) is for a set of the locations (A_3, A_4), $d_H = 4.99 \pm 0.01$ m, $d_L = 7.58 \pm 0.23$ m. The other combination of the emission locations $d_H = 4.29 \pm 0.01$, $d_L = 2.53 \pm 0.48$ gives rise to similar line profiles. The emission locations of $d_H = 4.99$ and 4.29 m correspond to the higher magnetic field $B = 3.46$ T. The locations of $d_L = 2.53$ and 7.58 m are the lower magnetic field $B = 2.55$ T. The Doppler shift velocity components along the tangential LOS are determined to be $v_H^{LOS} = 7.7 \pm 0.5$ km/s and $v_L^{LOS} = 2.0 \pm 1.5$ km/s at higher and lower magnetic field sides, respectively. The uncertainty includes an average of the two fitting results and fitting errors. If we assume that actual net ion motion is along the magnetic field, the velocities of ions are derived to be $v_H = 8.4$–8.6 km/s and $v_L = 2.4$–2.8 km/s from the angle ζ between the magnetic field direction and LOS as plotted in Fig. 3(e).

At this integrated time region $t = 0.612$–0.843 s, the NBI 2 of the clockwise direction mainly heats the plasma as shown in Fig. 4(b). The observed direction of ion velocity is opposite to the NBI 2 direction (see Fig. 1). At the next time window $t = 0.863 \sim 1.094$ s, NBI 1(ccw), NBI 2(cw), and NBI 3(ccw) sustain the plasma. The direction and the amount of the Doppler shifts change little as presented in Figs. 8(b) and 8(d). This persistent flow irrespective of the NBI mode suggests that the flow at the emission region may be a spontaneous flow induced by the nondiffusive momentum transport.[35,36]

[1] B. Edlén, Z. Astrophys. **22**, 30 (1942).
[2] B. Edlén, Phys. Scr. **T8**, 5 (1984).
[3] V. Kaufman and J. Sugar, J. Phys. Chem. Ref. Data **15**, 321 (1986).
[4] L. Yang and D. A. Church, Phys. Rev. Lett. **70**, 3860 (1993).
[5] L. Yang, D. A. Church, S. Tu, and J. Jin, Phys. Rev. A **50**, 177 (1994).
[6] E. Träbert, P. Beiersdorfer, S. B. Utter, G. V. Brown, H. Chen, C. L. Harris, P. A. Neill, D. W. Savin, and A. J. Smith, Astrophys. J. **541**, 506 (2000).
[7] E. Träbert, Can. J. Phys. **80**, 1481 (2002).
[8] I. Draganić, J. R. Crespo López-Urrutia, R. DuBois, S. Fritzsche, V. M. Shabaev, R. Soria Orts, I. I. Tupitsyn, Y. Zou, and J. Ullrich, Phys. Rev. Lett. **91**, 183001 (2003).
[9] E. Träbert, Phys. Scr. **72**, C42 (2005).
[10] A. Lapierre, U. D. Jentschura, J. R. Crespo López-Urrutia, J. Braun, G. Brenner, H. Bruhns, D. Fischer, A. J. González Martínez, Z. Harman, W. R. Johnson, C. H. Keitel, V. Mironov, C. J. Osborne, G. Sikler, R. Soria Orts, V. Shabaev, H. Tawara, I. I. Tupitsyn, J. Ullrich, and A. Volotka, Phys. Rev. Lett. **95**, 183001 (2005).
[11] S. Suckewer and E. Hinnov, Phys. Rev. Lett. **41**, 756 (1978).
[12] S. Suckewer and E. Hinnov, Phys. Rev. A **20**, 578 (1979).
[13] R. Katai, S. Morita, and M. Goto, J. Plasma Fusion Res. **7**, 9 (2006).
[14] M. J. Vilkas and Y. Ishikawa, Phys. Rev. A **68**, 012503 (2003).
[15] J. Gafert, K. Behringer, D Coster, C. Dorn, K. Hirsch, M. Niethammer, U. Schumacher, and the ASDEX Upgrade Team, Plasma Phys. Controlled Fusion **39**, 1981 (1997).
[16] R. C. Isler, N. H. Brooks, W. P. West, A. W. Leonard, G. R. McKee, and G. D. Porter, Phys. Plasmas **6**, 541 (1999).
[17] B. L. Welch, J. L. Weaver, H. R. Griem, W. A. Noonan, J. Terry, B. Lipschultz, and C. S. Pitcher, Phys. Plasmas **8**, 1253 (2001).
[18] H. Kubo, H. Takenaga, T. Sugie, S. Higashijima, S. Suzuki, A. Sakasai, and N. Hosogane, Plasma Phys. Controlled Fusion **40**, 1115 (1998).
[19] A. Kumagai, H. Kubo, H. Takenaga, S. Suzuki, K. Shimizu, N. Asakura, and M. Shimada, Plasma Phys. Controlled Fusion **42**, 529 (2000).
[20] T. Shikama, S. Kado, H. Zushi, A. Iwamae, and S. Tanaka, Phys. Plasmas **11**, 4701 (2004).
[21] T. Shikama, S. Kado, H. Zushi, M. Sakamoto, A. Iwamae, and S. Tanaka, Plasma Phys. Controlled Fusion **48**, 1125 (2006).
[22] A. Iwamae, M. Hayakawa, M. Atake, T. Fujimoto, M. Goto, and S. Morita, Phys. Plasmas **12**, 042501 (2005).
[23] Y. Takeiri, S. Morita, K. Tsumori *et al.*, Nucl. Fusion **45**, 565 (2005).
[24] S. Morita and M. Goto, Rev. Sci. Instrum. **74**, 2375 (2003).
[25] O. Motojima, H. Yamada, A. Komori *et al.*, Phys. Plasmas **6**, 1843 (1999).
[26] O. Kaneko, Y. Takeiri, K. Tsumori, Y. Oka, M. Osakabe, K. Ikeda, K. Nagaoka, T. Kawamoto, E. Asano, and M. Sato, Nucl. Fusion **43**, 692 (2003).
[27] T. Watanabe, Kaku Yugo Kenkyu, Bessatsu **63**, 482 (1990) (in Japanese).
[28] T. Watanabe, M. Yoshida, S. Masuzaki, M. Emoto, and Y. Nagayama, "How to use the numerical system LHD_LINES_OF_FORCE.EXE for the visualization of lines of force in the large helical device (Ver. III)" (http://dgegw3.nifs.ac.jp/documents/LHD_lines/manual_side-e.htm).
[29] T. Watanabe, Y. Matsumoto, M. Nishiki, S. Oikawa, H. Hojo, M. Shoji, S. Masuzaki, R. Kumazawa, K. Saito, T. Seki, T. Mutoh, A. Komori, and the LHD Experimental Group, Nucl. Fusion **46**, 291 (2006).
[30] Thorium-Argon Spectral Atlas (http://www.noao.edu/kpno/specatlas/thar/thar.html).
[31] M. Goto, S. Morita, K. Sawada, T. Fujimoto, S. Yamamoto, J. Miyazawa, H. Yamada, and K. Toi, Phys. Plasmas **10**, 1402 (2003).
[32] R. D. Cowan, *The Theory of Atomic Structure and Spectra* (University of California Press, Berkeley, 1981), p. 442.
[33] T. Fujimoto, F. Koike, K. Sakimoto, R. Okasaka, K. Kawasaki, K. Takiyama, T. Oda, and T. Kato, *Atomic Processes Relevant to Polarization Plasma Spectroscopy* (NIFS-DATA-16, 1992), pp. 60–81.
[34] K. Narihara, I. Yamada, H. Hayashi, and K. Yamaguchi, Rev. Sci. Instrum. **72**, 1122 (2001).
[35] K. Ida, Y. Miura, K. Itoh, S-I. Itoh, and T. Matsuda, J. Phys. Soc. Jpn. **67**, 4089 (1998).
[36] K. Ida, H. Yamada, H. Iguchi, K. Itoh, and the CHS Group, Phys. Rev. Lett. **86**, 3040 (2001).